Observation of fast-ion Doppler-shifted cyclotron resonance with shear Alfvén waves

Yang Zhang,[1] W. W. Heidbrink,[1] H. Boehmer,[1] R. McWilliams,[1] S. Vincena,[2] T. A. Carter,[2] W. Gekelman,[2] D. Leneman,[2] and P. Pribyl[2]

[1]*Department of Physics and Astronomy, University of California, Irvine, California 92697, USA*
[2]*Department of Physics and Astronomy, University of California, Los Angeles, California 90095, USA*

The Doppler-shifted cyclotron resonance ($\omega - k_z v_z = \Omega_f$) between fast ions and shear Alfvén waves is experimentally investigated (ω, wave frequency; k_z, axial wavenumber; v_z, fast-ion axial speed; Ω_f, fast-ion cyclotron frequency). A test particle beam of fast ions is launched by a Li$^+$ source in the helium plasma of the LArge Plasma Device (LAPD) [W. Gekelman, H. Pfister, Z. Lucky, J. Bamber, D. Leneman, and J. Maggs, Rev. Sci. Instrum. **62**, 2875 (1991)], with shear Alfvén waves (SAW) (amplitude $\delta B / B$ up to 1%) launched by a loop antenna. A collimated fast-ion energy analyzer measures the nonclassical spreading of the beam, which is proportional to the resonance with the wave. A resonance spectrum is observed by launching SAWs at $0.3 - 0.8\omega_{ci}$. Both the magnitude and frequency dependence of the beam-spreading are in agreement with the theoretical prediction using a Monte Carlo Lorentz code that launches fast ions with an initial spread in real/velocity space and random phases relative to the wave. Measured wave magnetic field data are used in the simulation. © *2008 American Institute of Physics.* [DOI: 10.1063/1.2996323]

I. INTRODUCTION

Fast ions are ions with energies that are much larger than typical thermal energies of plasma constituents. In laboratory experiments, fast ions are produced by neutral or ion beam injection,[1] by ion cyclotron[2] or lower hybrid heating,[3] and by fusion reactions. In astrophysical and space plasmas, instabilities and shocks generate fast ions.[4] Fast ions are also found when a hot plasma merges with a colder background plasma, as when the solar wind collides with the magnetosphere.[5]

Alfvén waves are also pervasive in both natural and laboratory plasmas. Alfvén waves constitute the dominant components of the electromagnetic wave spectra in the solar-terrestrial plasma environments and, consequently, can play crucial roles in mechanisms from solar corona heating to acceleration of charged particles in the solar wind,[5,6] aurora, and the Earth's radiation belts. Resonances between energetic particles and Alfvén waves are also suggested as one generating mechanism for the waves.

In many toroidal laboratory devices, Alfvén waves driven unstable by fast ions are observed with an intense fast-ion population. For example, the famous toroidicity-induced Alfvén eigenmode[7,8] (TAE) is the most extensively studied among numerous other modes excited by energetic particles.[9] Fast ions can also be expelled by these Alfvén instabilities and damage vessel components in fusion experiments.[10,11] Resonant heating of fast ions by Alfvén waves well below the ion cyclotron resonance frequency might cause ion heating in toroidal fusion devices.[9,12,13]

The interaction of fast ions with waves and instabilities is challenging to study experimentally because of difficulties in diagnosing the fast-ion distribution function and the wave fields accurately, in either hot fusion devices or space plasmas. Conventional experimental approaches are limited to noncontact, line or volume averaged methods in a tokamak, such as, various spectrometers and edge scintillators/ collectors for fast ions.[8] The Interplanetary Scintillation (IPS) array built at the Mullard Radio Astronomy Observatory was a representative remote diagnostics for monitoring the solar wind activities. Expensive spacecraft measurements near the earth can cover but a fraction of the daunting space influenced by the solar wind.

The approach of this work and the previous classical fast-ion transport study[14] is to launch test-particle fast-ion beams with a narrow initial distribution function in phase space using plasma-immersible fast-ion sources.[15,16] Here test-particle assumption is made since the background plasma density is much higher than the fast ion density. The unique LArge Plasma Device (LAPD) (Ref. 17) provides a probe-accessible plasma that features dimensions comparable to magnetic fusion research devices, which can accommodate both large Alfvén wavelengths and fast-ion gyro-orbits. The fast-ion beam is readily detected by a collimated fast-ion analyzer. With resonance overlap of fast ions and shear Alfvén waves (SAW), resonant beam transport, in addition to the well calibrated classical transport,[14] is analyzed with good phase-space resolution.

This paper presents the first direct experimental measurement of fast-ion cross-field transport induced by SAWs in the linear regime. The organization of this paper is as follows: In Sec. II, the analytical theory for this work is summarized with the results from single-particle and Monte Carlo Lorentz simulations. The experimental setup and fast ion/wave diagnostics are introduced in Sec. III. Major experimental results including observed fast-ion cyclotron resonance spectra are reported in Sec. IV. Conclusions are drawn in Sec. V along with suggestions for future studies of fast-ion transport in turbulent fields.

II. RESONANCE THEORY AND SIMULATION

A. Resonance models

A charged particle is in cyclotron resonance with a transverse wave if the oscillation of wave electric field $\widetilde{\mathbf{E}}$ matches the Doppler-shifted cyclotron motion of the particle,[18] when the particle and the wave exchange energy effectively. The condition for such a resonance between fast ions and SAWs propagating parallel to the ambient magnetic field $\mathbf{B_0}$ (along the z direction) is

$$\omega - k_z v_z \cong \pm \Omega_f, \tag{1}$$

where ω and k_z are the wave frequency and parallel wave number; v_z is the parallel velocity of the fast ions in the lab frame; and $\Omega_f = q_f B_0/m_f$ is the cyclotron frequency of the fast ions. For MHD shear Alfvén waves, the dispersion relation is $\omega = k_z v_A$ with $v_A = B_0/\sqrt{\mu_0 n_i m_i}$ as the wave phase velocity (the Alfvén speed), $n_i m_i$ is the mass density of the plasma. The upper/lower sign in Eq. (1) corresponds to the normal/anomalous Doppler resonance where fast ions travel slower/faster than the wave phase velocity along $\mathbf{B_0}$. In the following experiments, normal Doppler resonance is investigated. The goodness of the resonance is first evaluated by this normalized difference

$$\Delta\bar{\omega} = (\omega - k_z v_z - \Omega_f)/\Omega_f \ll 1. \tag{2}$$

The position $\mathbf{x}$ and velocity $\mathbf{v}$ of the fast ion is given by the Lorentz force law,

$$\frac{d\mathbf{v}}{dt} = \frac{q_f}{m_f}(\widetilde{\mathbf{E}} + \mathbf{v} \times \mathbf{B_0} + \mathbf{v} \times \widetilde{\mathbf{B}}),$$
$$\frac{d\mathbf{x}}{dt} = \mathbf{v}, \tag{3}$$

where $\widetilde{\mathbf{E}}$ and $\widetilde{\mathbf{B}}$ are the wave fields of SAW. Adopting Cartesian coordinates, the wave electric field can be modeled as linearly polarized in the y-z plane,

$$\widetilde{\mathbf{E}}(y,z,t) = (\widetilde{E}_y \hat{y} + \widetilde{E}_z \hat{z})\cos(\omega t - k_z v_z + \phi_0), \tag{4}$$

where φ_0 is the launched phase of the fast ion relative to the wave and assuming $\widetilde{E}_x = 0$. From Ampere's law, $\widetilde{E}_y$ is related to $\widetilde{B}_x$ through

$$\widetilde{E}_y = -\frac{k_z \widetilde{\mathbf{B}}_x}{\omega \mu \varepsilon}, \tag{5}$$

where $\mu\varepsilon$ is determined by the plasma dispersion relation (Sec. II B). In the experiment, $\widetilde{E}_y$ has a perpendicular pattern determined by the characteristics of the SAW antenna (see Sec. III D). Replace $\widetilde{\mathbf{B}}$ in Eq. (3), then the changes of fast-ion velocity components become

TABLE I. List of parameters for typical cases of fast ion and SAW resonance.

| Parameter | Resonance | | | |
	Li_7^+ Doppler (I)	Li_7^+ Doppler (II)	Li_7^+ Doppler (III)	Li+7 Landau
B (kG)	1.6	**1.74**	**1.2**	0.5
W (eV)	600	**600**	**600**	2000
θ (°)	29.5	**44.8**	**49.3**	15
ρ (cm)	2.9	**3.8**	**5.9**	8.2
Gyro-cycle/port	1/1	**4/3**	**1/1**	1/6
n_e (10^{12} cm^{-3})	2.0	**2.5**	**2.5**	4
T_e (eV)	6	**6**	**6**	4
f_{ci} (kHz)	610	**663**	**457**	191
Δr (cm) ($\Delta z = 0.96$ m)	0.43	**0.5**	**0.5**	n/a
Resonance $\bar{\omega}$	0.63	**0.63**	**0.65**	128

$$\frac{dv_x}{dt} = \frac{q_f}{m_f}(v_y \times B_0),$$
$$\frac{dv_y}{dt} = \frac{q_f}{m_f}\left[-v_x \times B_0 + \left(1 - \frac{\omega\mu\varepsilon}{k_z}v_z\right)\cdot\widetilde{E}_y\right], \tag{6}$$
$$\frac{dv_z}{dt} = \frac{q_f}{m_f}\left(\widetilde{E}_z + \frac{\omega\mu\varepsilon}{k_z}v_y\cdot\widetilde{E}_y\right),$$

which shows that perpendicular acceleration is only along the y direction, and that the parallel acceleration is associated with the rate of change of perpendicular kinetic energy,[18] as well as acceleration from $\widetilde{E}_z$. At the *exact* Doppler resonance condition, v_y grows linearly with t. The phase of $\widetilde{E}_y$ seen by the fast ion changes and eventually turns opposite, when the fast ion accelerates in the opposite direction. The amplitudes of the parallel and perpendicular velocities undergo slow oscillations over time and space much longer compared to the period and wavelength of the wave. This oscillation is actually the fast ion's trapping in the SAW. From Ref. 18, the trapping period ($\tau_{\rm trap}$) can be calculated as

$$\tau_{\rm trap} = \sqrt{\frac{8\pi m_f \omega}{k_z^2 q_f E_y v_{0z}}}, \tag{7}$$

where v_{0z} is the initial parallel velocity. The distance traveled along the z direction in $t_{\rm Trap}$ is defined as $\lambda_{\rm trap}$, the trapping length.

The Landau resonance is another resonance mechanism for the fast-ion beam to exchange energy with the SAW. The resonance condition for this case seems conceptually simpler than the Doppler resonance,

$$\omega - k_z v_z \cong 0. \tag{8}$$

However, it requires a fast Li$^+$ ion (>2 keV) at a relatively small initial pitch angle, which is currently not an operational regime for this thermionic emission source (see Sec. III B). One example of the Landau resonance condition is listed in Table I, where the plasma conditions are modified from usual LAPD operations in order to slow down the wave.

B. SAW dispersion relation

There are two regimes of plasma parameters for SAW propagation: the kinetic Alfvén wave (KAW) for plasma electrons having a Boltzmann distribution in the presence of the Alfvén wave fields and the inertial Alfvén wave (IAW) for electrons responding inertially to the wave. The KAW is more relevant to the physics of the interior regions of tokamak plasmas and the IAW to the edge and limiter regions. In this experiment, KAWs launched during the discharge of the LAPD are investigated.

A dimensionless parameter, $\bar{\beta}_e \equiv \bar{v}_{te}^2 / v_A^2$ is a quantitative measure of how inertial or kinetic a plasma is, where $\bar{v}_{te} = \sqrt{2T_e/m_e}$ is the thermal electron speed with T_e as the electron temperature. For example, if $\bar{\beta}_e \gg 1$, as the discharge plasma of the LAPD, it is kinetic; if $\bar{\beta}_e \ll 1$, as the afterglow plasma, is inertial. For the KAW, the dispersion relation is

$$\omega^2/k_\parallel^2 = v_A^2(1 - \bar{\omega}^2 + k_\perp^2 \rho_s^2), \qquad (9)$$

where $k_\parallel$ is the component of the wave vector parallel to the background magnetic field, $k_\perp$ is the perpendicular wave number, and ρ_s is the ion sound gyroradius [$\rho_s = c_s/\omega_{ci}$ with $c_s = (T_e/m_i)^{1/2}$]. The intensity of the parallel wave electric field is[33]

$$\widetilde{\mathbf{E}}_\parallel = \frac{i\omega k_\perp^2 \rho_s^2}{v_A(1 - \bar{\omega}^2)(1 - \bar{\omega}^2 + k_\perp^2 \rho_s^2)^{1/2}} \widetilde{\mathbf{E}}_\perp. \qquad (10)$$

A typical ratio of $|\widetilde{E}_\parallel/\widetilde{E}_\perp|$ is 0.01, which means that the non-vanishing parallel electric field will slightly modify v_z in the resonance experiment. The perpendicular electric field can be calculated from Ampère's law and the dispersion relation,

$$\left| \frac{\widetilde{\mathbf{E}}_\perp}{\widetilde{\mathbf{B}}_\perp} \right| = \frac{v_A(1 - \bar{\omega}^2)}{(1 - \bar{\omega}^2 + k_\perp^2 \rho_s^2)^{1/2}}. \qquad (11)$$

C. Single particle simulation

If the cross field transport of the test-particle beam is much smaller than the scale length of the wave fields, then a single-particle Lorentz code is capable of predicting the expected resonance beam profile by launching particles at an ensemble of initial phases (φ_0) relative to the wave. In the plasma physics literature, cross-field diffusion usually refers to radial transport of guiding centers. In this experiment, the fast ions only execute a few Larmor orbits prior to measurement, so it is conceptually simpler to examine the full helical Lorentz orbit rather than the guiding-center orbit.

A typical Doppler resonance fast-ion trajectory is shown in Fig. 1(a). Fast ion and wave parameters (Table I) are chosen to satisfy the Doppler resonance condition of $\Delta\bar{\omega} < 0.1$, using feasible experimental conditions. To indicate the relative strength of different SAWs, B_{max} is defined as the maximum amplitude of $\widetilde{B}_x$ in a specific z plane. If $\widetilde{B}_x = B_{max}\hat{x}$ at $t=0$, the ions, initiated in phase with the wave, would lose energy [Fig. 1(b)] continuously to the wave and the magnetic moment ($\mu = mv_\perp^2/2B$) decreases. At several gyro-cycles away in the z direction, the fast-ion energy (W) and μ changes linearly with the traveling time/distance; as W
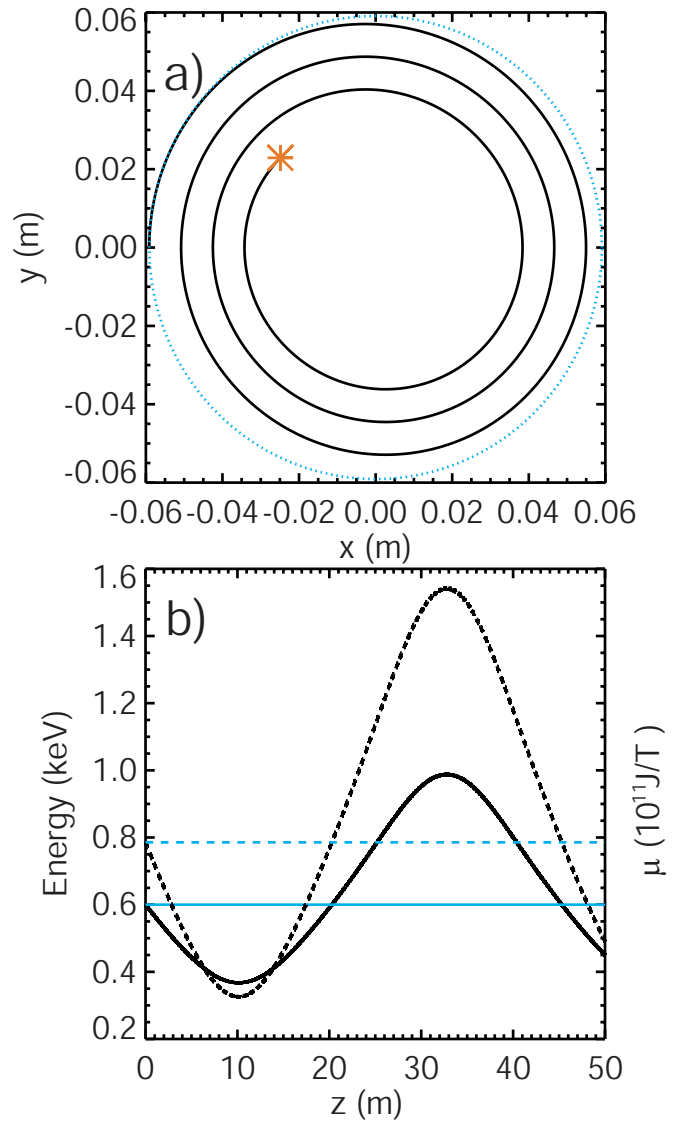

FIG. 1. (Color online) Single-particle simulation results: (a) An x-y projection of SAW influenced gyro-orbit (solid black) is compared with the unperturbed one (dotted cyan). The orbit originates from $(-0.06,0)$ and ends at the red star; $B_{max}=10$ G; (b) fast-ion energy (solid) and magnetic moment (dashed) trapping in the SAW. Horizontal lines represent the unperturbed value. $B_{max}=1$ G. ($\varphi_0=0$, fast-ion parameters refer to Doppler resonance case III in Table I.)

changes, the initial phase φ_0 will eventually change to $\phi_0 \pm \pi$, when W starts to change in the opposite direction. In this case, the trapping length (λ_{trap}) is ~46 m from the original z position [Fig. 1(b)]. The fast ion oscillates in phase space over long periods, which demonstrates the trapping of fast ions in the wave frame.

If an ensemble of ions are launched with random phases relative to the wave, $\phi_0 \in [0, 2\pi]$, other initial conditions being identical, their positions on the collection plane mark the spatial spreading due to the perturbation from the wave field [Fig. 2(a)]. The maximum displacements from the undisturbed position along the $\hat{r}$ and $\hat{\varphi}$ directions are defined as Δr and $r_0\Delta\Phi$. It is obvious that Δr is a direct indicator of the change in perpendicular ion energy ($W_\perp$). The gyro-phase Φ
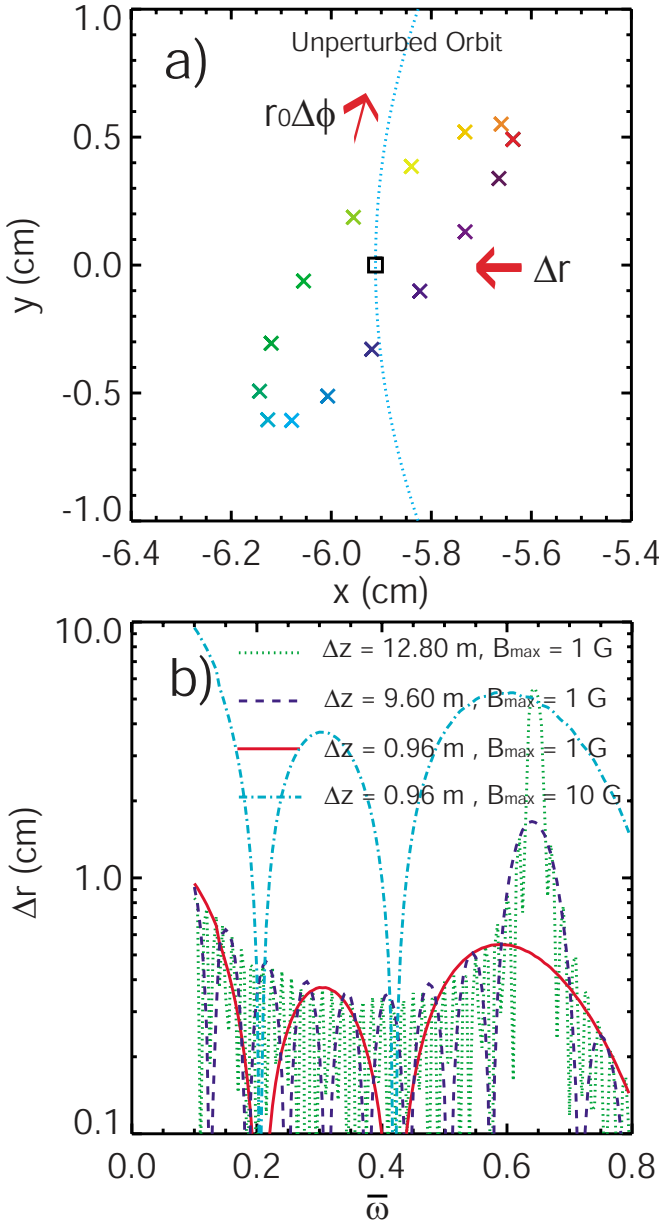
FIG. 2. (Color online) Single-particle simulation results, contain (a) fast ion collection positions at $\Delta z = 0.96$ m with 16 uniformly distributed values of initial wave phase $\varphi_0 \in (0, 2\pi)$ (color crosses). Black box is the unperturbed collection position; $B_{max} = 1$ G; (b) radial shift Δr vs normalized antenna frequency for different values of z and B_{max}. (Fast-ion parameters refer to Doppler resonance case III in Table I.)

TABLE II. Comparison of time rates for different transport mechanisms; $B_0 = 1.2$ kG.

Transport time scales	Time (ms)
Pitch angle scattering: τ_{PAS}	5
Coulomb energy-loss: τ_W	1
SAW period: τ_{SAW}	0.002—0.02
Cyclotron motion: $\tau_{Cyclotron}$	~0.003

factor of the resonance is degraded but a clear maximum is still observed. The spatial displacements are proportional to the SAW wave field amplitude, as expected for moderate field perturbations ($\delta B/B < 1\%$) in the linear regime.

The simulation code was first used to find the optimal conditions for conducting the resonance experiments with fast-ion sources in the LAPD. Realistic parameters listed in Table I are evaluated in the code for $\Delta\bar\omega$, Δr, and $r_0\Delta\Phi$. Those sets of parameters satisfying $\Delta\bar\omega \ll 1$ while producing observable Δr and $r_0\Delta\Phi$ are selected for experiments at the LAPD. Three lithium fast-ion Doppler resonance conditions in Table I are realized and measured experimentally. In this article, if not otherwise specified, the resonance parameters are for Li_7^+ Doppler resonance case (III).

D. Monte Carlo simulation

Since the single-particle model cannot simulate a finite beam with spatial and energy distributions, an existing Monte Carlo fast-ion orbit code[19] is upgraded to include the SAW-induced fast-ion transport, as well as the classical transport caused by thermal ions and electrons. In the LAPD discharge plasma, the electrons dominate Coulomb slowing-down, while thermal ions dominate the pitch-angle scattering rate. A number of fast ions are launched numerically according to the initial beam divergence in phase space ($\pm 5°$ in pitch angle and ~ 5 eV in energy). Due to the difference in time scales of the transport mechanisms shown in Table II, the classical transport effects can be readily decoupled from the SAW influence in the code.

During the simulation of each fast-ion orbit, the pitch angle scattering event is considered at a randomly selected time ($t = t_1$), by which each gyro-period is divided into two partitions ($\tau_{Cyclotron} = t_1 + t_2$). Figure 3 shows the flow chart of the simulation process. The single-particle Lorentz code is carried on throughout t_1 and t_2 for SAW perturbation. At the end of each time partition, the fast-ion energy is updated by the Coulomb slowing-down effect,

$$W' = W \exp\left(-\frac{t}{\tau_W}\right). \qquad (12)$$

At $t = t_1$, a Monte Carlo collision operator[19] developed from the Coulomb scattering theory[20] is loaded to scatter the direction of the fast-ion velocity without changing its magnitude. After the desired number of gyro-periods is finished, the fast-ion velocity and coordinates are recorded in the computer memory and the next fast ion is launched.
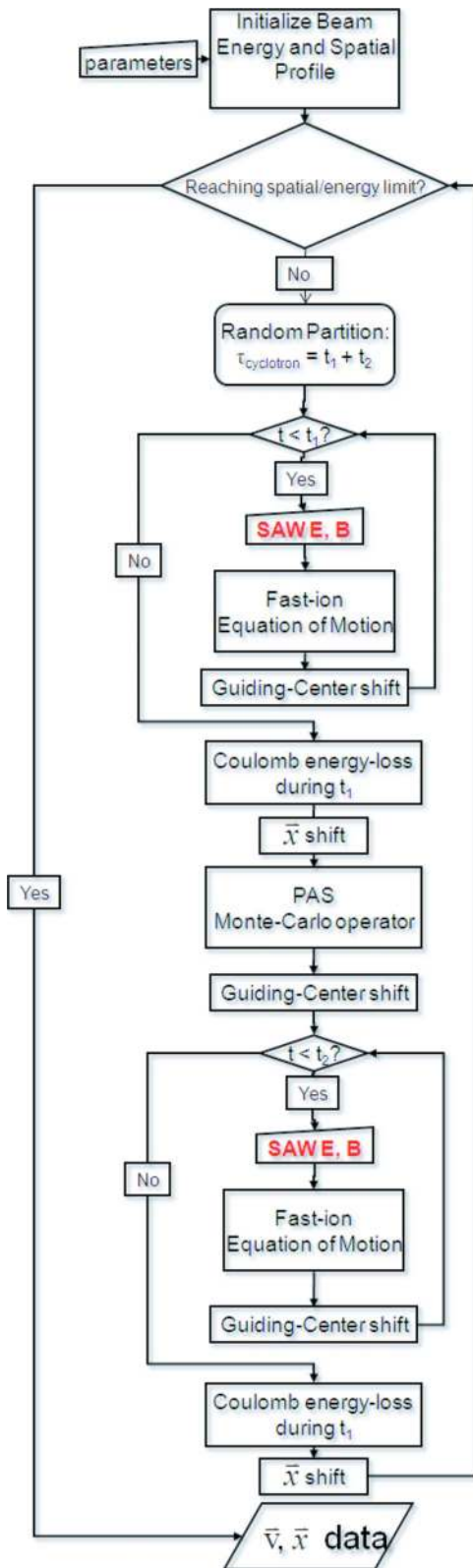
at the collection plane is $\Omega_f \Delta z / v_z$, where Δz is the distance traveled by fast ions in the z direction. Thus $r_0\Delta\Phi$ indicates the change in parallel energy ($W_\parallel$).

In the simulation, varying the wave frequency from 0.1 to $1.0\omega_{ci}$ (singly ionized helium ion cyclotron frequency), one can obtain a spectrum of spatial displacements caused by SAW perturbations. In Fig. 2(b), Δr and $r_0\Delta\Phi$ are plotted against $\bar\omega = \omega/\omega_{ci}$, where the frequency satisfying the resonance condition ($\Delta\bar\omega = 0$) is 0.65 ω_{ci}. Resonance spectra show that the maximum displacement occurs at the expected frequency. At larger Δz (less than $\lambda_{trap}/4$), the resonance frequency is closer to $0.65\omega_{ci}$ and the resonance peak is sharper. At shorter lengths, e.g., several gyro-cycles away, the quality

FIG. 3. (Color online) Monte Carlo simulation flow chart.

the classical profiles at different distances traveled by fast ions. Notice in Fig. 4, all the fast ions collected in the x-y plane are included regardless of their final velocities. The classical beam profile produced by a 0.5 cm diameter source aperture is shown in Fig. 4(a). For the SAW-perturbed beam profiles, B_{max} is set at 10 G. At the resonance peak frequency [Fig. 4(b), $\bar{\omega}=0.65$], substantial profile widening happens along both the $\hat{r}$ (gyro-radius) and $\hat{\varphi}$ (gyro-angle) directions. The widening effect increases with the distance traveled by the fast ion. At the resonance null frequency [Fig. 4(c), $\bar{\omega}=0.20$], on the contrary, fast ions only perform drifting motions along with the guiding center, whereas the gyro-radius as well as the perpendicular energy does not change much. At $\Delta z=0.32$ m and 0.64 m, beam profiles at different phase (φ_0) form ellipses in the z plane. At $\Delta z=0.96$ m, where fast ions finish three gyro-cycles, the beam profile [Fig. 4(c)] has minimal drifting and is close to the unperturbed one in Fig. 4(a). The experimental findings in Sec. IV agree with these results from the Monte Carlo model.

III. EXPERIMENTAL SETUP

A. Overview

This experiment is performed in the upgraded LAPD, which has a 17.56-m-long, 1-m-diam cylindrical main vacuum chamber. Pulsed plasmas ($\sim$10 ms in duration, 1 Hz repetition rate, and $\pm10\%$ spatial uniformity) are created by a discharge between a barium oxide coated cathode and a gridded molybdenum anode.[21] The cathode and anode are separated by 50 cm and both located at the south end of the machine. The working gas is helium at a partial pressure $\sim3\times10^{-5}$ Torr with less than 3% of impurities. Typical average plasma parameters for this experiment are $n_i\sim2.5\times10^{12}$ cm^{-3}, $T_e\sim6$ eV, $T_i\sim1.0\pm0.5$ eV. The fast-ion beam density (5.0×10^8 cm^{-3}) used in this experiment is typically three to four orders of magnitude smaller than the plasma density, which ensures the test-particle assumption.

Figure 5(a) illustrates the hardware configurations for this experiment. The origin of the z axis is defined as the location of the lithium fast-ion source (Sec. III B). The beam-wave interaction region is $\sim$10 m downstream of the cathode to ensure radially uniform background plasma properties. The SAW antenna (Sec. III D) is located at $z=-3.52$ m to avoid the near field effect (typical SAW wavelength parallel to $\mathbf{B}_0$ is $\sim$4 m). The fast-ion analyzer (Sec. III B) scans fast-ion signals in the x-y plane 0.32–0.96 m away from the source to vary the interaction time between wave and particle. Figure 5(b) shows the actual LAPD port locations of all the instruments relative to the ambient magnetic field profile. The distance between two adjacent ports is 0.32 m. One set of magnets next to the anode-cathode carries a higher current corresponding to a 1.4 kG field to avoid strong Alfvén maser formation[22] that would otherwise become a major source of noise. A dissipating magnetic beach on the north end of the machine is used to suppress reflections of the waves at the end of the machine. The axial magnetic field profiles are calculated from the actual current distribution for all the magnets in the

Using the same linearly polarized shear Alfvén wave fields as for the single-particle simulation, thousands of fast-ion orbits are launched with random phases (φ_0) to contribute to the beam profile several gyro-cycles away. The SAW-perturbed beam profiles are compared in Fig. 4 with
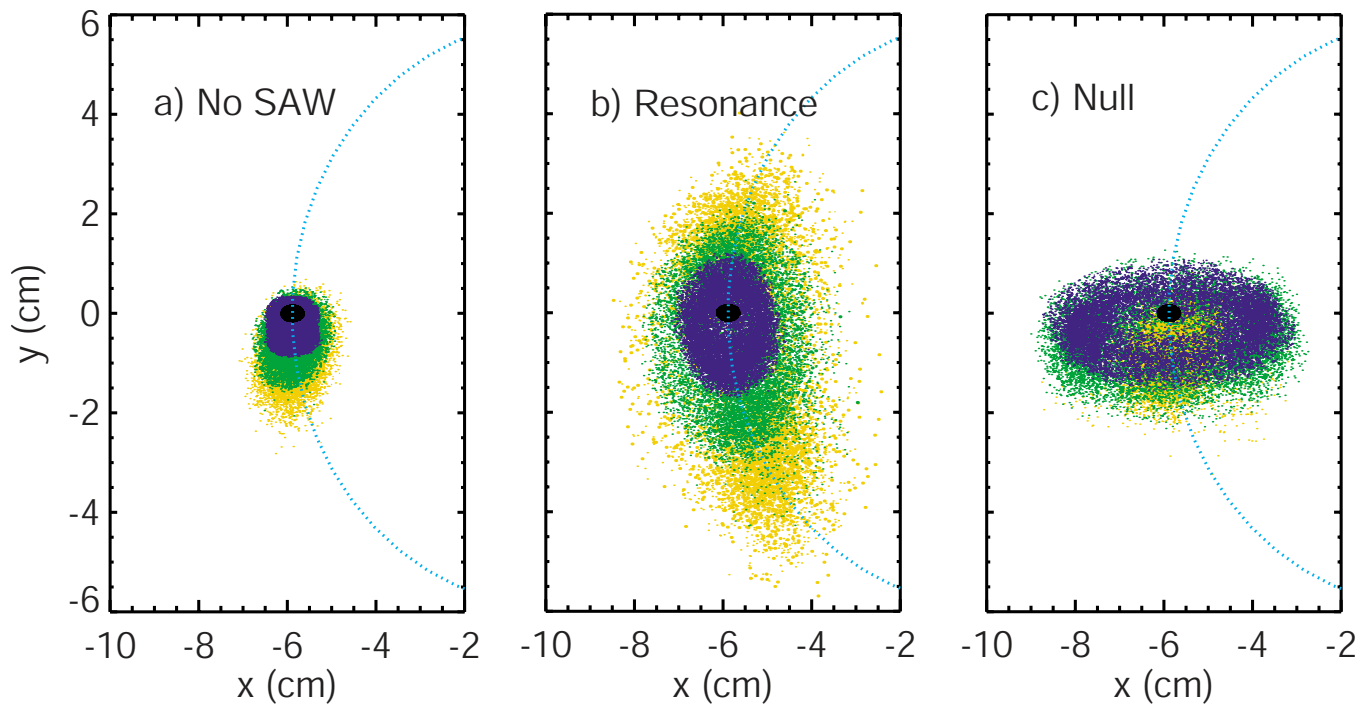
FIG. 4. (Color online) Monte Carlo model simulated fast-ion beam profiles with different SAW perturbations. The color of the dots indicates fast ion collection at different z planes: black ($\Delta z=0$ m), blue ($\Delta z=0.32$ m), green ($\Delta z=0.64$ m), and orange ($\Delta z=0.96$ m). (a) No SAW present; (b) SAW at $\bar{\omega}=0.65$ (resonance peak), $\tilde{B}_x=10$ G; (c) SAW at $\bar{\omega}=0.20$ (resonance null), $\tilde{B}_x=10$ G. (Cyan dotted curves are the unperturbed fast ion orbit.)

machine.[23] The estimated axial field ripple amplitude at the radius of the machine is less than 2% for a constant field configuration.

B. Lithium fast-ion source and diagnostics

Lithium ion sources[15] with lithium aluminosilicate as thermionic emitters of different sizes (0.6 in. and 0.25 in. diameter, Heat Wave Inc.[24]) were designed, constructed, and characterized at UC Irvine. For this transport study, the 0.6 in. emitter version with isotopically purified Li-7 (99.99% grade, experimentally determined to be greater than 90%, Ref. 25) is operated with a 5 mm diameter circular aperture to achieve a narrow, high uniformity beam. Typical beam current densities are in the 1 mA/cm^2 range at beam voltages between 400 V and 2000 V determined by the emitter bias. The source is placed into the LAPD vacuum chamber from a side vacuum-lock (port 35). Beam propagation in the LAPD is facilitated by sufficient charge neutralization from the plasma. On the other hand, strong cathode electron current (~2 A/cm^2) streaming down the magnetic field damages the lithium emitter and poses a heavy load on the emitter bias power supply. Thus a minimum pitch angle of 28° is required for the fast-ion orbit design to avoid line-of-sight between the emitter and the cathode. The emitter lifetime is about 20 h for the aforementioned typical operation.

The stainless steel outer-shield (3 in. $\times$ 5 in.) of the source changes local plasma parameters (especially when the outer shield is grounded to the LAPD chamber as preferred). A measurement of plasma floating potential (V_f) near the source region shows up to 10 V of decrease, which causes a small adjustment of the beam energy. SAWs launched from inserted antennas can also be influenced if the source is aligned axially with the oscillating current channels that create the wave (Sec. III D).

Synchronization between the lithium source and the LAPD plasma is arranged so that the ~20 ms fast-ion pulse is turned on and off every two plasma discharges, with an adjustable delay and duration. The background signal is taken when the source is disabled for one shot right after the previous beam-on shot. An even number of shots is repeated at one spatial location before the probe drive moves on. The signals with the source off are subtracted from the signals with the source on. The fast-ion signals shown in this work are net signals with background subtractions.

An electrical diagram for the experiment is shown in Fig. 6. Apart from the Alfvén Maser signal, which is usually avoided as stated earlier, there exist two major noise sources: the ~6 kA plasma discharge pulse causes ringing signals at 1–1000 Hz due to capacitive and inductive couplings; and the SAW rf driving-circuit generates EM noise outside of the chamber. It is thus very important for the lithium source to have a solid ground reference to the LAPD chamber ground with a complete shield around the heating and biasing circuit. Two Mu-metal shielded high-voltage power supplies[26] bias the emitter and the accel-decel grid at desired voltages with $<0.05\%$ ripple rate (<0.3 V_{pp} ripple at 600 V), monitored by a Tektronix P6015A high voltage probe.

After the beam travels in the plasma and wave fields, a collimated fast-ion analyzer is employed to produce a good fast-ion signal-to-noise in strong rf noise environment during the LAPD discharge. It packages a 3.2 mm diam collector, an identical dummy for differential amplification, and three
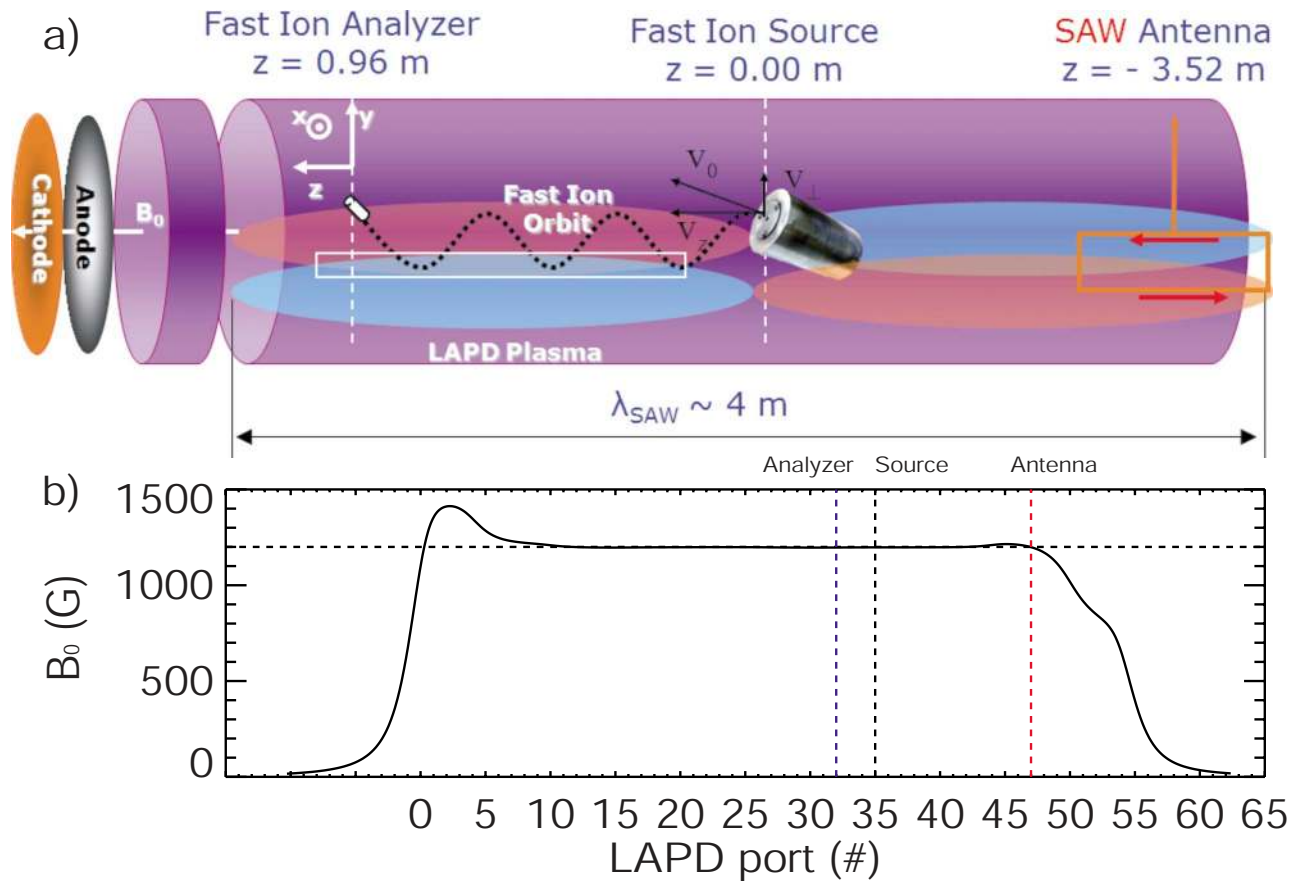
FIG. 5. (Color online) Experimental setup at the LAPD. (a) Overview of instruments (dotted helix is the fast ion orbit; white box denotes the fast ion-SAW interaction region); (b) ambient magnetic field profile vs LAPD port number (black solid). The distance between two adjacent ports is 0.32 m. Instruments' typical locations are marked by dashed perpendicular lines.

molybdenum grids for variable electrical barriers.[15] The fast-ion current and the dummy pickup signal are fed through a RG 178B/U coaxial cable twisted pair, shielded by the stainless 0.95 cm O.D. shaft. Due to the shaft length that is required by the LAPD standard probe drive as well as a minimum of ~1 m for external connection, the total capacitance of each coaxial signal line is ~270 pf. For this work, a 1 MΩ input resistance is needed for sufficient fast-ion signal as well as for rf-pickup rejection. Signals are preamplified by a Lecroy DA1822A differential amplifier. A SONY/Techtronix A6907 optical isolator separates the fast-ion current reference and the data collection ground, reduces the offset caused by the plasma discharge, and amplifies the beam signal for the 100 MHz, 14 bit digitizer.

Measurements of the beam profile and wave field utilize a 2D probe drive system (±0.5 mm precision) and take advantage of the highly reproducible plasma of the LAPD. At each spatial location, multiple time traces are collected with a number of plasma shots repeated. The probe tip is then moved to the next spatial position according to the preselected grid and the process is repeated. A typical fast-ion profile during the discharge of the LAPD plasma is reconstructed from the data array and shown in Fig. 7. The collimated fast-ion analyzer has both good fast-ion signal-to-noise and spatial resolution.

C. Basic beam profile analysis

For this transport study, fast-ion parameters are always selected to complete integer numbers of gyro-cycles that coincide with the location of diagnostic ports since the slightly divergent beam is only refocused at integer numbers of gyro-orbits, as described by the "geometrical effect" in Ref. 14. The beam originates from the circular aperture, experiences classical cross-field diffusion, and passes the collection x-y plane with a pitch-angle θ close to the initial value.

Energy spread of the fast-ion beam contributes to the elongation in the direction of gyro-motion. The variation in gyro-phase with energy can be expressed as

$$\Delta\phi = \sqrt{\frac{m_f}{8W^3}}\frac{\Omega_f \Delta z}{\cos\theta}\Delta W, \qquad (13)$$

where ΔW is the variation of fast-ion energy perpendicular to the fast-ion source exit face. For a typical 20 eV emitted energy spread, Doppler resonance case III and $\Delta z = 0.96$ m, the variation is 11° in gyro-phase and 1.2 cm in beam width along the $\hat{\varphi}$ direction, which is considerably larger than the wave electric field induced spread. In contrast, the radial beam width is determined primarily by the radius of the
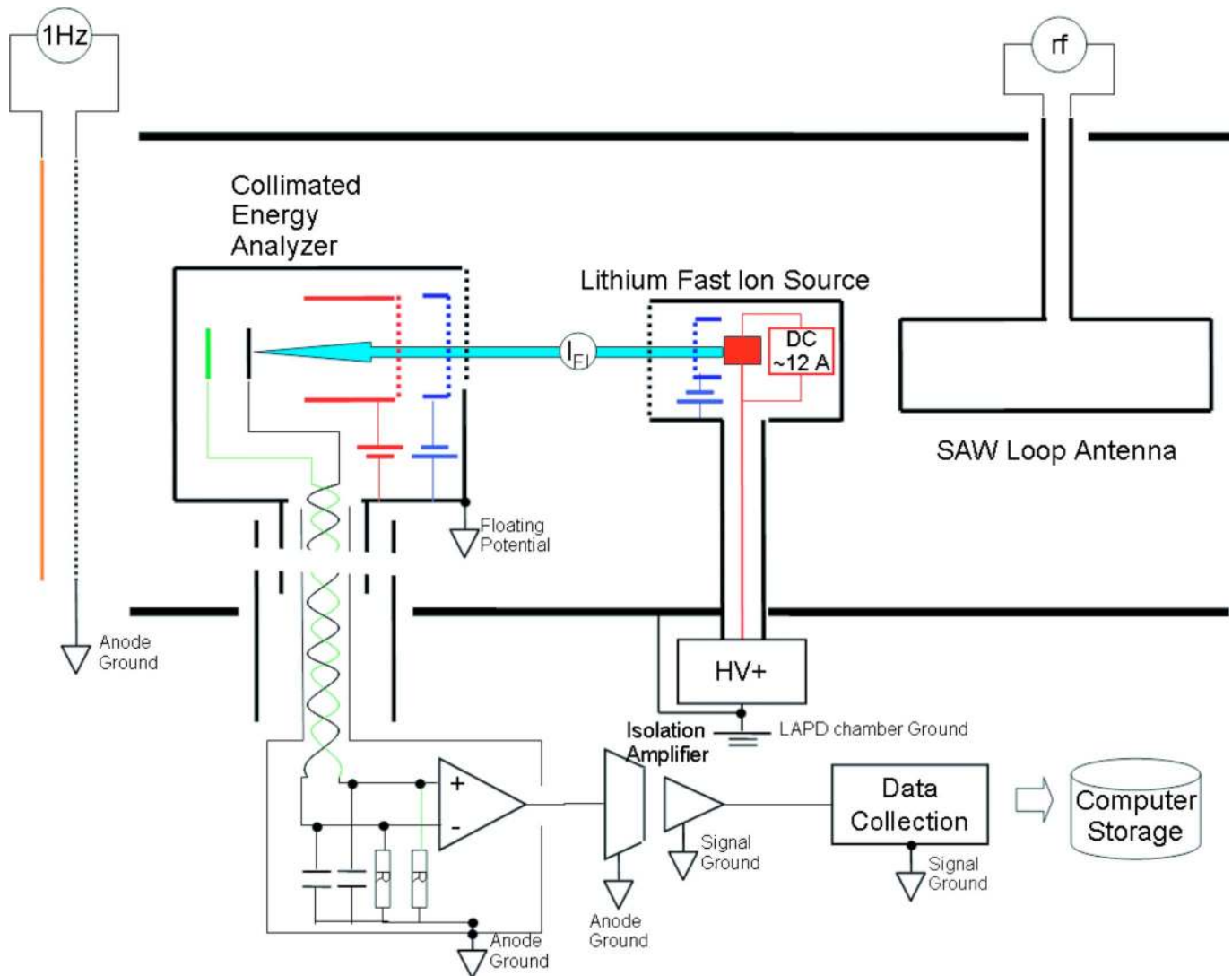
FIG. 6. (Color online) Electrical configurations and shielding solutions for fast-ion generation and diagnostics. (Drawings are not to scale.)

aperture (0.5 cm). Since the radial beam profile has the benefit of being less influenced by the initial beam energy spread and classical transport effects, it is favored in the data analysis (Sec. IV).

The curvature of the gyro-orbit at the beam collection point causes a small portion of the beam to be absorbed on the wall of the probe before reaching the recessed collector, which is the vignetting effect discussed in Ref. 27. Since the analyzer is always rotated in the y-z plane to match the incoming beam, the effective collector size in the gyro-direction is close to the original diameter of 3.2 mm. The effective collector size in the radial direction is determined to be ~ 2.7 mm by a simulation of an ensemble of fast-ion orbits in the analyzer geometry in the x-z plane. If a perfect 5 mm diameter beam is collected in this manner, the widths of the beam along the radial and gyro-directions, convoluted with the effective collector size, are 5.7 mm and 5.9 mm, respectively.

The beam 2D signal array from the analyzer is processed with statistical weights to yield the profiles along radial and gyro-directions separately (Fig. 7). First the beam trajectory

is fitted in the x-y plane with the given radius, using Gaussian centers of all the rows of data along the x direction. Then the profile data are projected along radial lines and fitted to Gaussian distributions with the goodness of fitting (χ^2) recorded as statistical weights. Finally the total weighted average radial profile is obtained as well as the gyro-profile (Gaussian peak values along the gyro-direction). The fact that the radial profile is close to a Gaussian distribution is consistent with diffusive spreading, as expected and observed for classical transport.[14]

D. Launching SAW in the LAPD

The LAPDs large physical size and sufficiently high plasma density and magnetic field accommodates multiple Alfvén wavelengths. Research on SAW properties in the LAPD dates back to 1994 when pairs of theoretical[28,29] and experimental[30,31] papers were published on SAWs radiated from small perpendicular scale sources in the LAPD. Subsequently, other mechanisms were discovered to generate Alfvén waves including a variety of inserted antennas, reso-
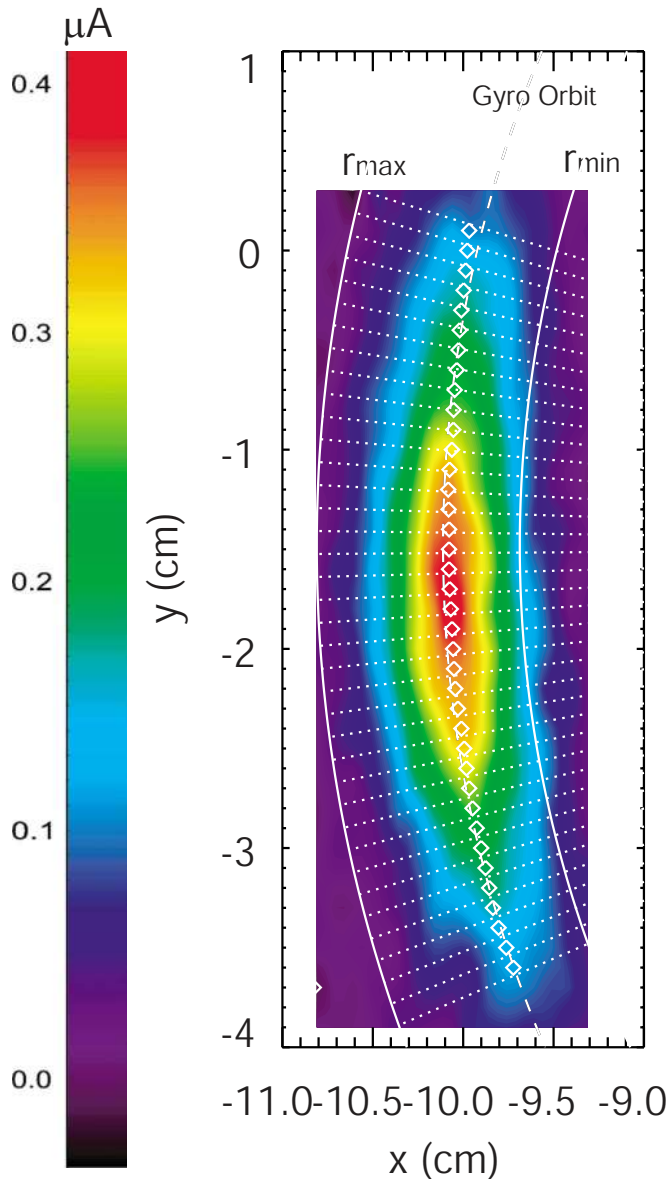
FIG. 7. (Color online) A typical lithium fast-ion beam profile during the discharge of the LAPD plasma, with superimposed curves to aid further analysis. Fast-ion analyzer located at $z=0.96$ m. (White diamonds: Gaussian center of x profiles; white-dashed: fitted gyro-orbit from Gaussian centers; white dotted: radial lines every 1°; white-solid: minimum and maximum radial range.)
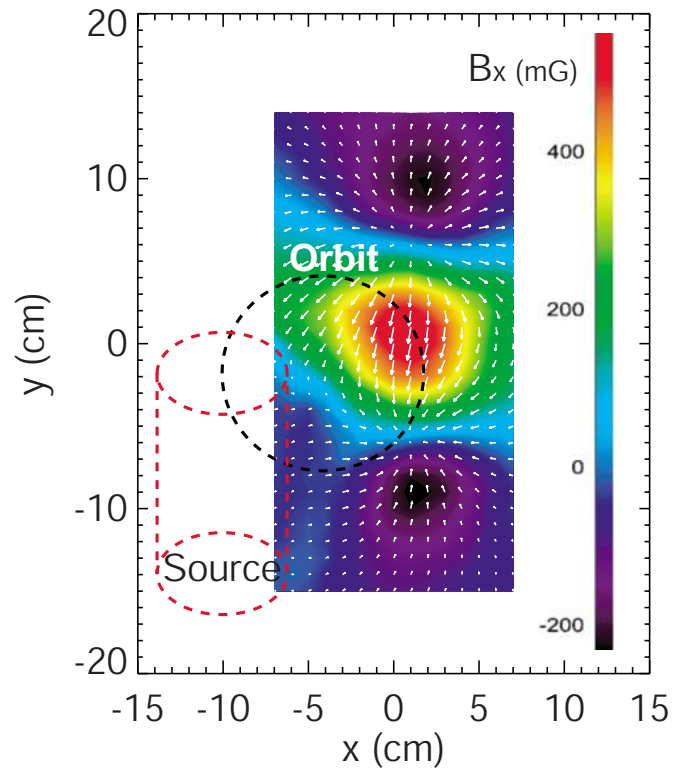

FIG. 8. (Color online) The x-y plane arrangement of fast-ion source (red dashed) and the SAW fields viewing from the cathode. Electric field data (white arrows, length proportional to field intensity, maximum at 34.3 V/m) are calculated from the measured magnetic field data ($\widetilde{B}_x$ shown by color contour) taken at $z=0.64$ m, $f=297$ kHz. The unperturbed fast-ion orbit is the black dashed circle. Red dashed cylinder represents the geometry of the source.

nance between the LAPD cathode, and the semitransparent anode—the Alfvén Maser,[22] and a dense laser-produced plasma expansion.[32] In 2005, Palmer[33] measured thermal ion polarization and $\widetilde{\mathbf{E}} \times \mathbf{B}_0$ drifts caused by SAW fields.

This work uses an insulated rectangular copper loop[34] as the antenna. It is 30 cm along $\mathbf{B}_0$ and 15 cm along the y axis. Currents flowing through the two parallel wires along $\mathbf{B}_0$ generate a double-channel perpendicular field pattern. The linearly polarized region of the pattern is aligned with part of the gyro-orbit to produce the Doppler resonance effect. Figure 8 shows the typical alignment of the Li$^+$ orbit and the SAW fields in the x-y plane, where the resonant fast ion gets a "kick/drag" every time it "swings" by the maximum field region. Notice white arrows are calculated wave electric

fields [Eq. (11)]. The geometry and position of the source head is also drawn to show that, for larger gyro-orbit condition, the source head is farther away from the SAW current channels and has less effect on the fields.

Two different circuits drive the loop antenna. The primary rf supply drives up to 2 kA through the loop and generates Alfvén wave amplitudes up to 10 G at variable frequencies up to 0.8 ω_{ci} (Fig. 8). An Ethernet controlled Agilent waveform-generator manages the frequency of the output SAWs. The current wave form is triangular and contains harmonics of the fundamental. Since the SAWs are expected to be strongly damped near and above ω_{ci},[35] the harmonics are usually inconsequential but do affect waves launched at fundamental frequencies lower than 0.3 ω_{ci} (Sec. IV C). The secondary driving circuit produces a clean sine wave form but requires matching capacitances for each SAW frequency. It produces amplitudes up to 1 G. In the following, the default antenna current drive is the triangle one unless otherwise noted.

The fluctuations of the $\widetilde{B}_x$ spectrum (Fig. 9) as $\bar{\omega}$ varies are due to the field-line-resonance effect studied by Mitchell et al.[36,37] Although a flaring field at the north end of the machine is configured to reduce this effect [Fig. 5(b)], there are still reflected waves to interfere with the primary waves. The b-dot probes measures the linear addition of all wave fields. Since only the forward wave can satisfy the normal
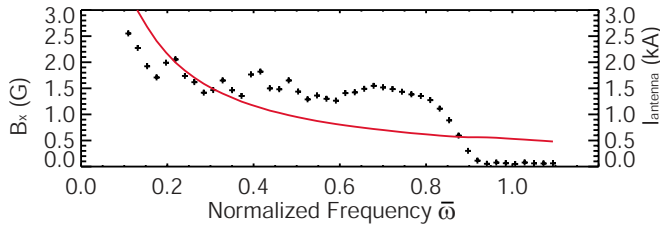
FIG. 9. (Color online) Spectra of $\widetilde{B}_x$ and loop antenna current by triangle drive. *b-dot* probe signal taken at the radial center of $z=-0.32$ m during the Sep. 2007 LAPD run (black cross: $\widetilde{B}_x$ intensity at each frequency; red solid: antenna current) (Data acquired with 100 MHz sampling rate, averaging 8 samples and 8 consecutive plasma shots).

Doppler resonance condition, using the *b-dot* probe measured fields for Doppler resonance calculation would incur moderate systematic error ($<10\%$).

E. SAW signal detection and processing

The wave magnetic field is measured by a set of identically designed *b-dot* probes featuring three orthogonal, differentially wound induction coil-pairs which are sensitive to the time derivative of the wave magnetic field.[38] Each coil-pair is connected to a differential amplifier to select magnetic signal and reject common mode noise along each axis.

The SAW antenna current I_{ant} and the three components of the SAW field ($\widetilde{B}_i$ as the *i*th component) signals are processed using a cross-covariance algorithm,

$$\langle \widetilde{B}_i(L) \rangle = \frac{\sum_{k=0}^{N-|L|-1} (\widetilde{B}_{ik+|L|} - \bar{\tilde{B}}_i)(I_{antk} - \bar{I}_{ant})}{\sqrt{\sum_{k=0}^{N-1}(I_{antk} - \bar{I}_{ant})^2/N}}, \quad L<0, \quad (14)$$

where N is the length of the array, L is a variable lag between $\widetilde{B}_i$, and I_{ant}, $\bar{\tilde{B}}$, and $\bar{I}_{ant}$ are the averaged rms values, k

represents the index of the time-sequence array. Since the magnetic signal train is excited linearly to the antenna current with only a delay in time, the lag that yields the first maximum of the cross-covariance is interpreted as the propagation time of the wave from the antenna to the *b-dot* probe. More importantly, the wave phase variation across the whole scanning plane is preserved in $\langle \widetilde{B}_i(L) \rangle$ and thus the wave field perpendicular pattern is recovered by combining the $\langle \widetilde{B}_i(L) \rangle$ results at each grid point (Fig. 10).

Measurements of *b-dot* in the *x-y* plane at multiple ports show that the axial variations of the wave field perpendicular pattern are small for the same launching frequency. The influence of the grounded fast-ion source on the wave pattern is noticeable and frequency scans reveal different levels of this effect on the wave pattern near the source. Higher frequency SAWs, corresponding to shorter parallel wavelengths, have more distortion in the wave pattern (Fig. 10).

IV. SAW-INDUCED FAST-ION TRANSPORT RESULTS

A. Fast-ion signal shows SAW-induced transport

As discussed earlier, the ~ 20 ms fast-ion beam pulse is turned on and off every two LAPD plasma discharges. Close to the end of each discharge, the plasma parameters reach the best uniformity in time and space, when the loop antenna drives an adjustable rf current for $0.5-0.8$ ms, launching SAWs at the specified frequency. The beam pulse overlaps in time with the 10 ms LAPD discharge. The data collection time-window opens for 2 ms with ~ 0.5 ms before and after SAW duration. A typical time history of a Doppler resonance experiment is shown in Fig. 11, with SAWs launched at the resonance frequency (297 kHz for Doppler resonance case III). The triangle wave form of the SAW current is magnified
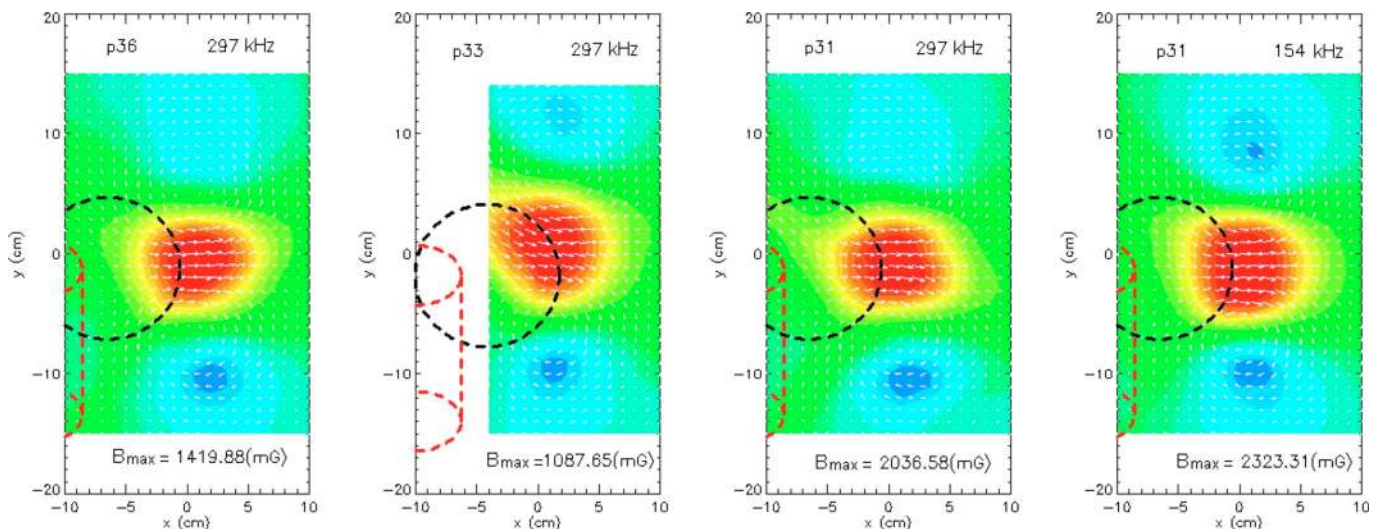

FIG. 10. (Color online) Perpendicular SAW magnetic field patterns. (a) Port 36 ($z=-0.32$ m), $f=297$ kHz; (b) port 33 ($z=0.64$ m), $f=297$ kHz; (c) port 31 ($z=1.28$ m), $f=297$ kHz; (d) port 31 ($z=1.28$ m), $f=154$ kHz. (White arrows: magnetic field vectors; color contour: $\widetilde{B}_x$ intensity; black dashed circle: unperturbed fast-ion orbit; red dashed cylinder: fast-ion source.)
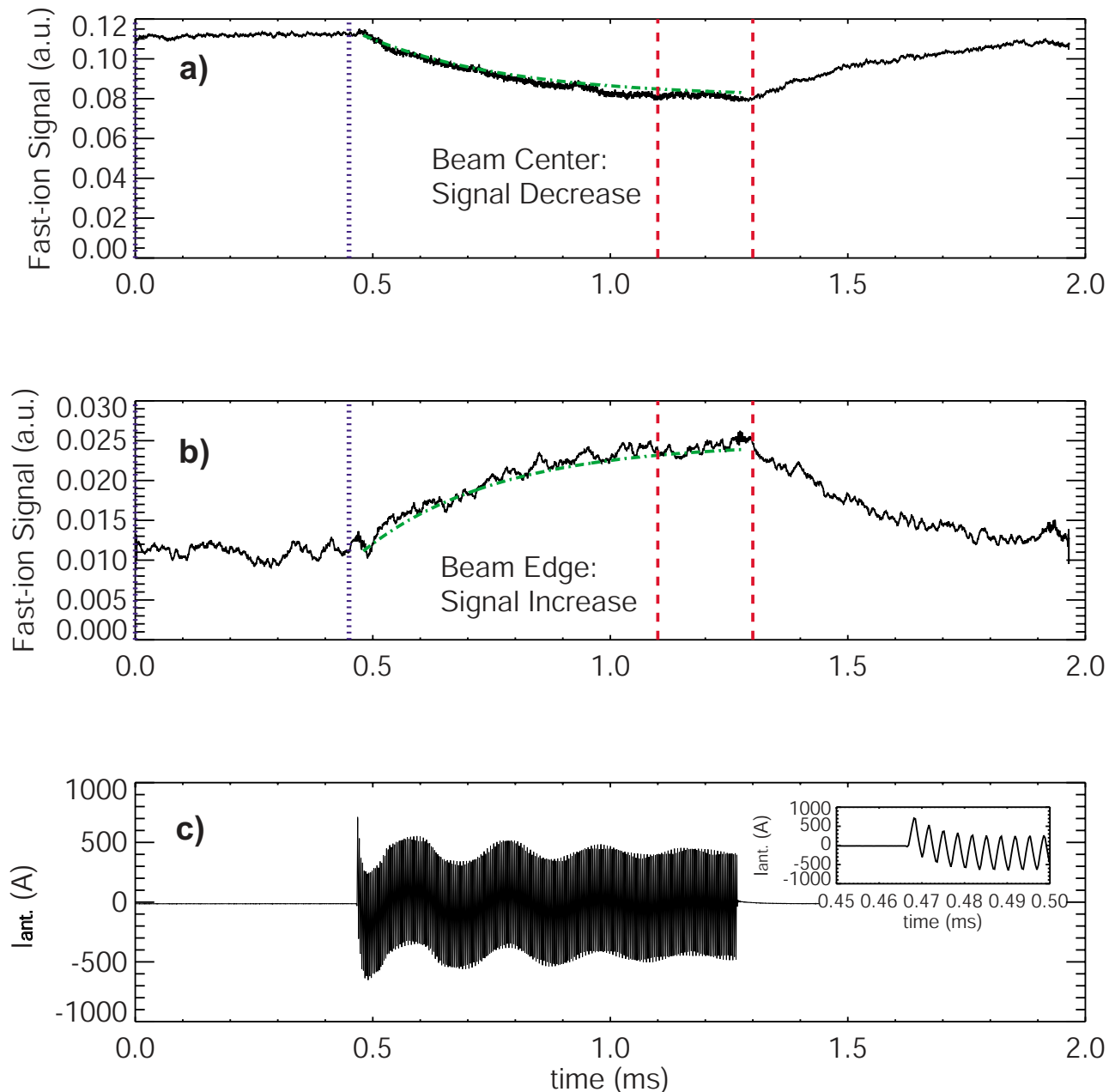
FIG. 11. (Color online) Typical fast-ion signal time traces influenced by SAWs at the Doppler resonance frequency. (a) Beam center signal RC decay; (b) beam edge signal RC rise; (c) loop antenna current. Inset: magnified triangle current signal for the initial 0.5 ms. (Black solid: data; green dotted-dashed: fitted curves; blue dotted: time domain for no-SAW data; red dashed: time domain for with-SAW data) (SAW frequency 297 kHz; data acquired with 25 MHz sampling rate, averaging 8 samples and 8 consecutive plasma shots, Dec. 07 LAPD run).

in the inset of Fig. 11(c). Fast-ion net signals are shown in Figs. 11(a) and 11(b) where the source is pulsed on for the whole ~2 ms window.

The fast-ion signals in Figs. 11(a) and 11(b) change significantly in time when SAWs propagate to the location of the fast-ion orbit several microseconds after current drives through the antenna. The spatial locations of the two time traces are different: a) is taken at the center of the beam spot, whereas b) is near the edge. Since the RC time is much longer than the SAW period, fast-ion signal variation at the SAW frequency is filtered out. However the averaged beam profile would still widen in the $\hat{r}$ and $\hat{\varphi}$ directions, as shown in the Monte Carlo simulation results (Fig. 4). With particle

conservation in mind, the fast ions are transported from the center of the beam to the edge, during Doppler resonance. This effect in the experiment is shown in Fig. 11 where the beam center/edge signal decreases/increases with the SAW on. When the SAW stops propagating several microseconds after the antenna current is turned off, the signal returns to the unperturbed levels. The green curves in Figs. 11(a) and 11(b) are the fitted RC decay/rise curves yielding a RC time of 0.3 ± 0.05 ms, which is in agreement with the calculated RC time.

In the following analysis, the SAW-influenced beam signal uses the averaged signal from 0.6 ms after the onset of the antenna current, shown in Figs. 11(a) and 11(b) with the
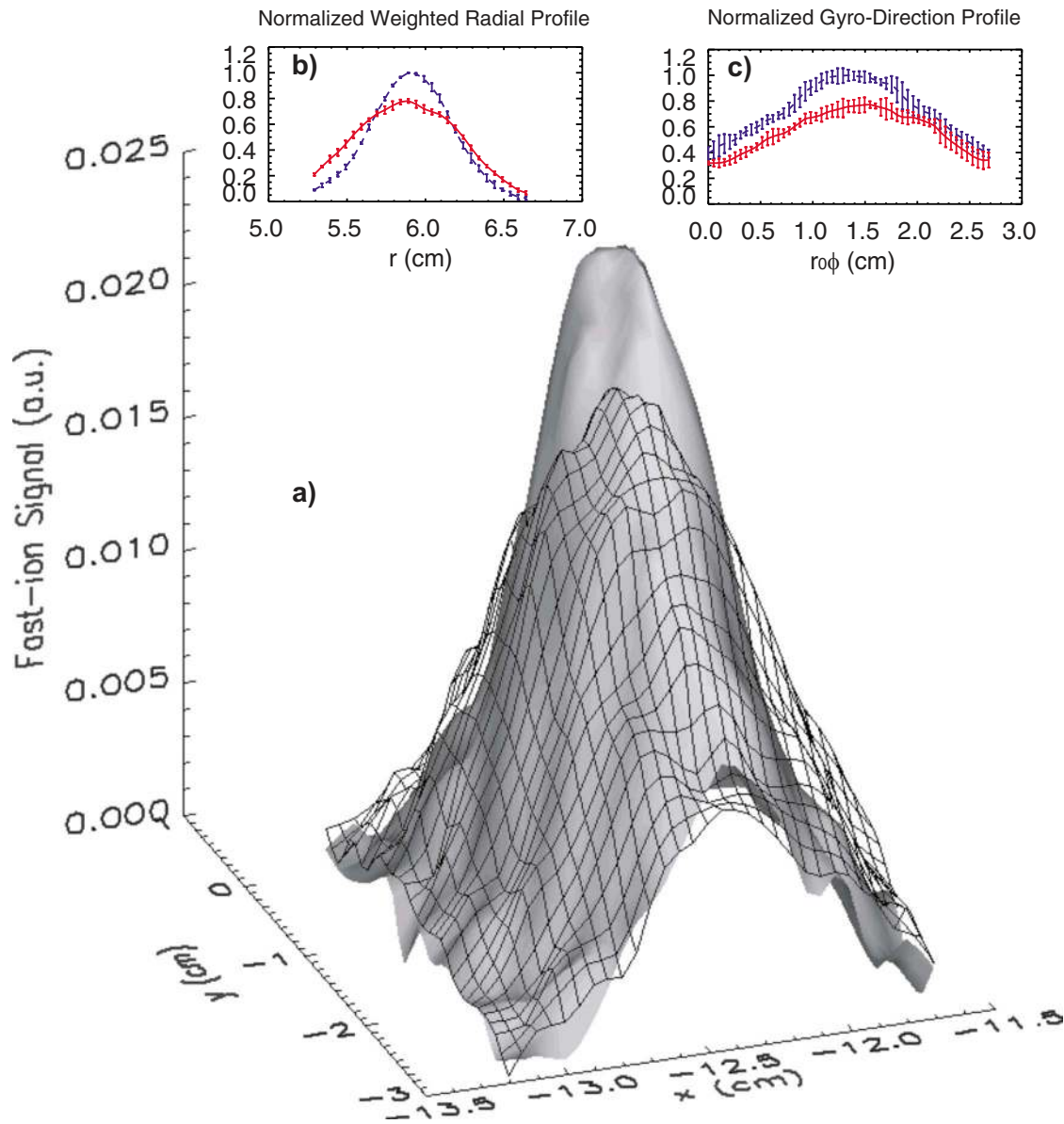
FIG. 12. (Color online) Comparison of fast-ion beam profile with and without SAW influence. (a) 3D visualization of beam profiles with (gridded surface) and without (shaded surface) SAW influence. (b) Normalized weighted radial profiles with (red solid) and without SAW influence (blue dashed). (c) Normalized gyro-direction profiles with (red solid) and without SAW influence (blue dotted) (SAW frequency 297 kHz; data acquired with 100 MHz sampling rate, averaging 8 samples and 10 consecutive plasma shots, Sep. 07 LAPD run).

red-dashed time window. This average underestimates the change if the SAW-influence time was infinite, which means the actual fast-ion transport effect in the experiment is up to $\sim 8\%$, which is more significant than that shown by the current data. The unperturbed beam signal, as a reference, is the average over the blue-dotted time window before SAW influence.

Time traces taken at a selected spatial grid are processed to show the fast-ion beam profile at the x–y plane. Fast-ion signals with and without the SAW influence show significant differences [see Fig. 12, in agreement with the transport effect at resonance frequency, from the 3D visualization in Fig. 12(a)]. Fast-ion intensity migrates from the center of the beam to the edge, causing widening along the $\hat{r}$ and $\hat{\varphi}$ directions. The beam profile along each direction is

acquired using the statistical technique mentioned in Sec. III C. Both profiles are widened as the SAW is turned on.

B. Measured Doppler resonance spectra

In this section, quantitative agreement between the measured and predicted resonant spatial broadening is demonstrated by comparing measured resonance spectra of SAW-induced displacements to the theoretical spectra.

Based on the theoretical spectrum [Fig. 2(b)], a set of SAW frequencies is selected to cover the important features including peaks and nulls of the resonance. For each of these frequencies, the antenna is driven for multiple plasma shots (8–10) and fast-ion signals are taken at the same spatial lo-
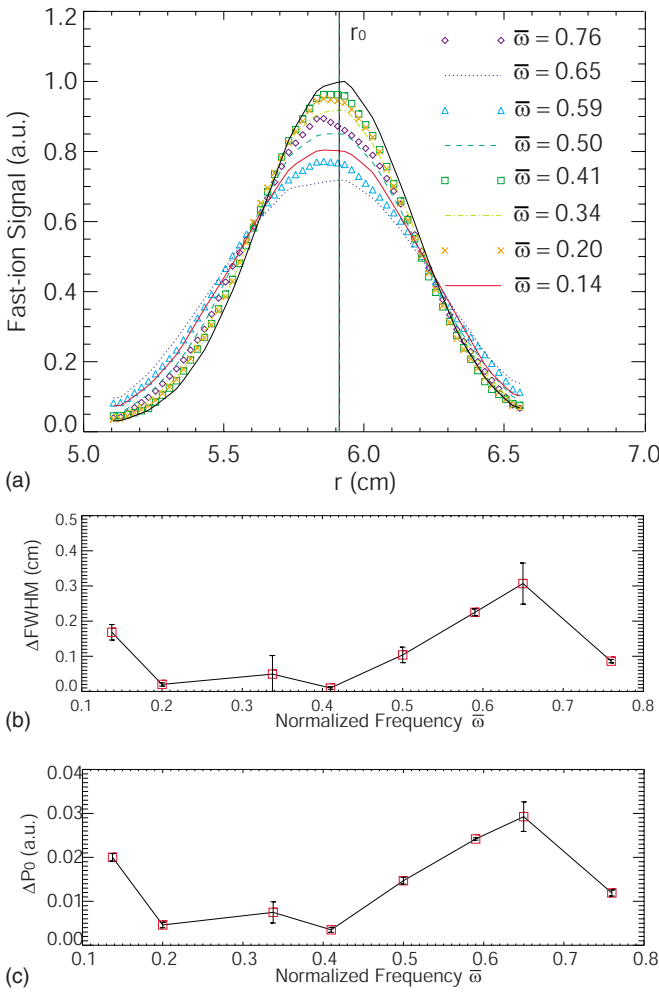
(a)

(b)

(c)

FIG. 13. (Color online) (a) Fast-ion beam radial profiles with various SAW frequencies (colored lines/symbols) compared to the unperturbed profile (black solid). (b) Change in FWHM of beam radial profiles vs SAW frequency; (c) change in Gaussian peak intensity (P_0) vs SAW frequency. (Data acquired with 25 MHz sampling rate, averaging 8 samples and 8 consecutive plasma shots, Dec. 07 LAPD run.)

cation. After completing all the frequencies and shots, the fast-ion analyzer is moved to the next point on the x-y grid. The total time of the spectra measurement is usually kept within 2 h ($\sim 1/10$ of source lifetime) to avoid significant change in the lithium source performance.

The spatial profile at each frequency is acquired from the data array and analyzed as shown in Fig. 7. As mentioned in Sec. II, both Δr and $r_0 \Delta \Phi$ are measurable indicators of the resonance effect and Δr is more favorable, which corresponds to the change in the perpendicular fast-ion energy. In Fig. 13(a), a typical set of radial profiles for the selected frequencies (colored) are shown, to which the classical profile (black-dashed) is compared. The fast-ion migrating effect varies as the frequency, which peaks at 0.65 ω_{ci} and attenuates at 0.20 and 0.41 ω_{ci}, as expected from the theory. In Figs. 13(b) and 13(c), the frequency dependencies of the full-width-half-maximum (FWHM) and the beam intensity coefficient (P_0) calculated from the Gaussian fit of the profile are plotted,
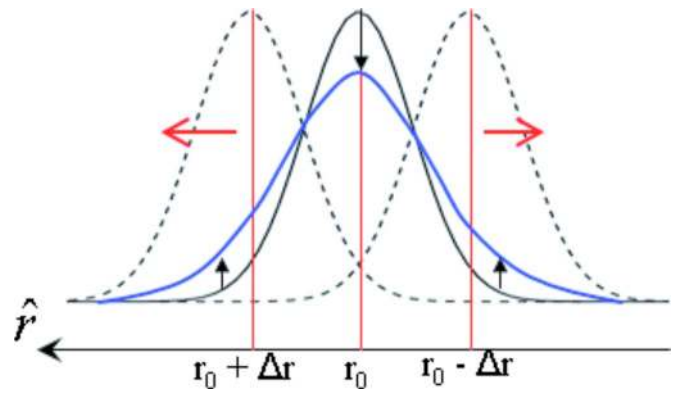

FIG. 14. (Color online) Illustration of widened beam spot caused by beam displacement along the $\hat{r}$ direction.

$$P(r) = P_0 \exp\left[- \frac{(r - r_0)^2}{b^2} \right] + P_c, \tag{15}$$

where P is the radial profile, b is proportional to the FWHM, and P_c is the background level. It is obvious that the variations of both quantities have similar dependence on $\bar{\omega}$ as expected.

In order to determine Δr quantitatively from the experimental beam profile, the profile WITHOUT SAW is displaced digitally to find an empirical Δr that produces the best fit of a specific profile WITH SAW. The single-particle result in Fig. 2(a) shows that the fast-ion collection position undergoes elliptical displacements with SAW perturbations at different phases (φ_0). The projection of the SAW displaced beam center (r_{SAW}) along the $\hat{r}$ direction can be thus modeled by

$$r_{SAW} = r_0 + \Delta r \sin(\varphi_0), \tag{16}$$

where r_0 is the classical radial position and Δr is as defined in Sec. II. Then the integration of all the displaced profiles across the region of $\phi_0 \in [0, 2\pi]$ yields an empirical profile that is dependent on Δr. If such a profile has the best χ^2 fit to a SAW perturbed profile, then the corresponding Δr is regarded as the displacement inferred from experimental data (Fig. 14). For well-behaved Gaussian distributions like the beam classical profiles in Eq. (15), that integration can be written as

$$P(r, \Delta r) = \frac{1}{2\pi} \int_0^{2\pi} \left(P_0 \exp\left\{ - \frac{[r - r_0 - \Delta r \sin(\omega t)]^2}{b^2} \right\} + P_c \right) d\varphi_0. \tag{17}$$

This algorithm converges rapidly as φ_0 integration step goes below $2\pi/100$.

Figure 15 shows the Doppler resonance spectra of calculated Δr from measured fast-ion beam profiles. For Doppler resonance case III, two different sets of data acquired during two LAPD runs (Sep. and Dec. 2007) and are plotted in Fig. 15(a), both using the triangle wave drive at similar intensities. The single-particle model using a generic wave field pattern with scalable B_{max} produces the continuous
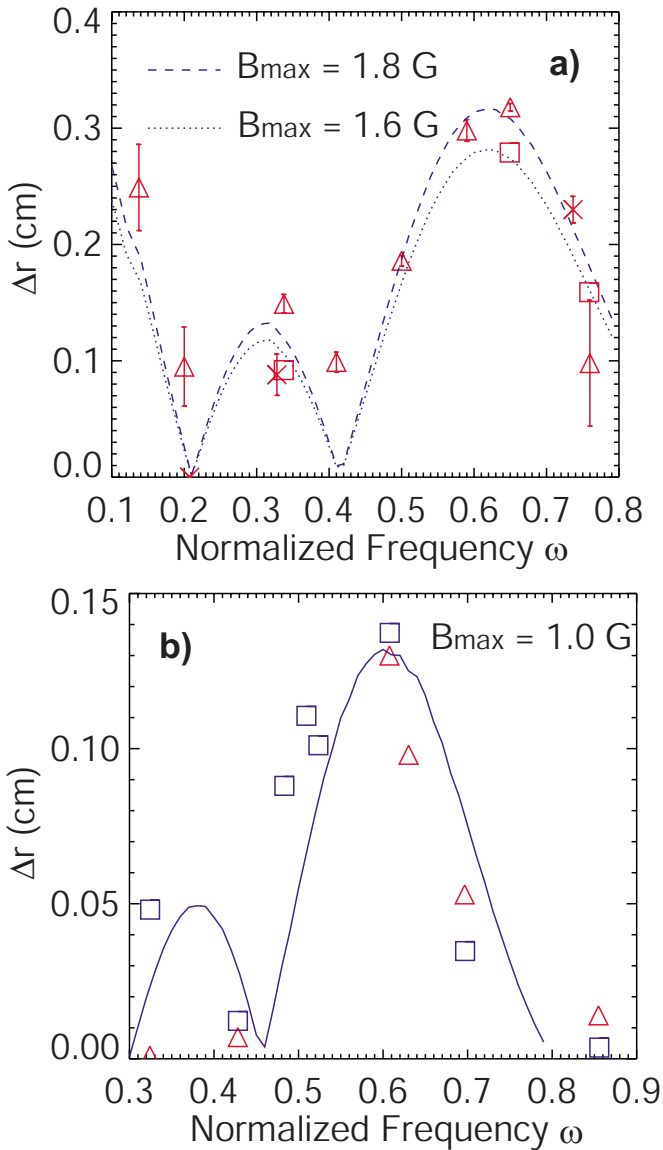
FIG. 15. (Color online) Doppler resonance spectra: experimental (red) and theoretical (blue). The blue boxes are the calculated displacements using experimental wave magnetic field data and the blue curves are the theoretical resonance from the single-particle model. (a) Doppler resonance case III ($\rho = 5.9$ cm) with triangular wave current drive. Red triangles: $B_{max} = 1.8$ G (Dec. 2007 LAPD run); red boxes: $B_{max} = 1.6$ G (Sep. 2007 LAPD run); red crosses: sinusoidal wave current drive. (b) Red triangles: Doppler resonance case II ($\rho = 3.8$ cm) with triangular wave current drive (Sep. 2007 LAPD run).

theory curve. Although slightly different in the wave field strength and the source-antenna arrangement between the Sep. and the Dec. run, the resonance spectrum is similarly characterized by both data sets. The absolute magnitude of Δr shows good agreement between experiment and theory except for the null point (see Sec. IV C). In Fig. 15(b), Doppler resonance case II is plotted with its own theoretical resonance curve. Agreement is still good even though this case has smaller fast-ion gyro-radius (3.8 cm) and the source has more perturbation on the SAW field pattern (Fig. 10).

The error bars in Fig. 15 are random errors calculated among data taken at 8 consecutive LAPD shots. During each shot, 5000 samples are averaged to get beam signal at one spatial location, with and without SAW. The highly repeatable plasma-fast-ion-SAW system contributes to the miniscule random errors. Potential systematic errors that include the source-antenna alignment is routinely done with a telescope through a glass viewport at the north end of the LAPD with ± 1 mm error. The *b-dot* probe measurements at multiple ports along fast-ion trajectory ensures the wave perpendicular pattern is centered at the antenna center with ± 1 cm error. The errors in the fast-ion initial mean energy (600 ± 1 eV) and pitch angle ($49.3 \pm 0.2°$). The $\sim 10\%$ of fluctuation in the wave magnetic field spectrum caused by the field-line-resonance modes. However, none of these error sources can contribute to the nonlinear resonance spectrum in Fig. 15, especially with the nulls and peaks observed experimentally.

C. Multimode versus single-mode SAW

The odd-numbered harmonics contained in the triangle waveform of the wave fields can also contribute to the SAW-induced fast-ion transport. It is obvious in Fig. 15(a) that Δr does not become a complete null at ~ 0.20 ω_{ci} as predicted by the theory curve, with single-mode SAW fields. A multimode SAW simulation as well as displacement measurements with the sine wave drive are thus necessary to address this effect.

To describe the triangle wave, an infinite Fourier series can be used,

$$B_x(t) = \sum_{k=1}^{\infty} B_k \cos(k\omega t + k\pi - \pi), \tag{18}$$

where k is always an odd number, B_k is the intensity of the kth harmonic. For the same fundamental frequency, the FFT intensity of each harmonic stays comparable until it rises above 0.8 ω_{ci} [Fig. 16(a)], where the intensity of the wave magnetic field rolls off quickly. For example, the third harmonic can be effective for fundamental frequencies up to ~ 0.3 ω_{ci} and the seventh up to ~ 0.13 ω_{ci}. The SAW spectrum in Fig. 9 is used to determine the intensity of each harmonic relative to the fundamental. Harmonics are added one by one to the fundamental, shown by different curves in Fig. 16(b). The theory curve (red-solid) with up to the seventh harmonic included fits of the experimental results the most, with the maximum normalized to the peak experimental displacement.

A good null point at 0.20 ω_{ci} is measured with the clean single-mode SAW driven by the sine wave drive. The displacements measured with the sine-wave drive at 0.20, 0.33, and 0.73 ω_{ci} are reported in Fig. 16(b) as red diamonds. The maximum wave amplitude driven by the sine wave drive is close to 80% of the triangle wave.

V. CONCLUSIONS AND FUTURE WORK

In this experimental work, the Doppler-shifted cyclotron resonance effect is directly measured from the beam spatial nonclassical spreading caused by single and multimode shear Alfvén waves. Both qualitative and quantitative agreements of the SAW-induced spatial displacements with theory are
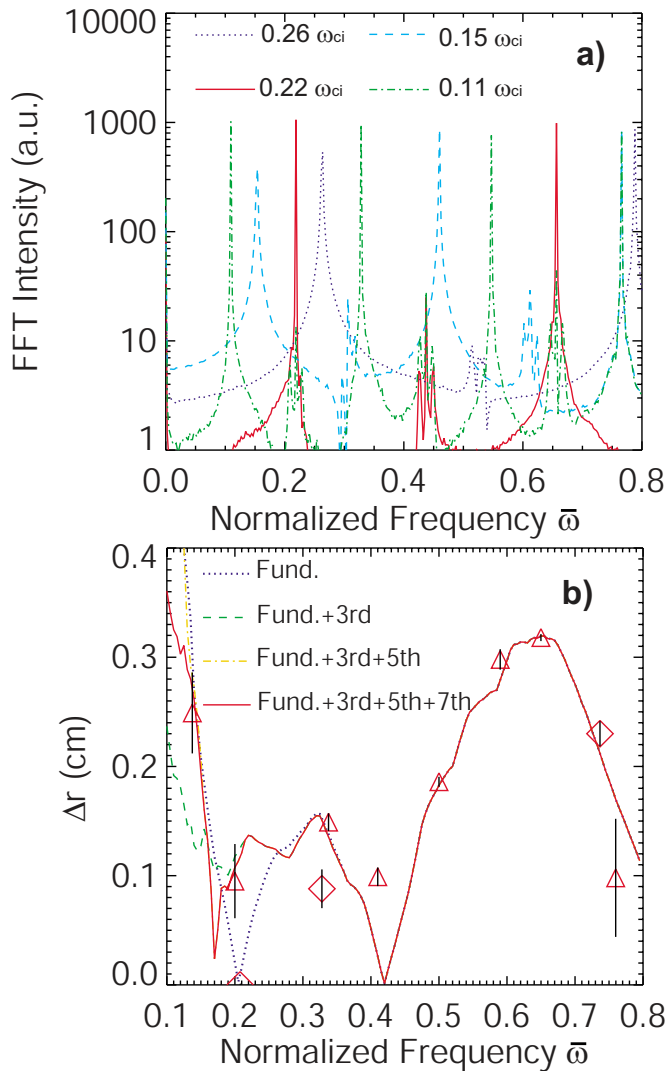
FIG. 16. (Color online) (a) Typical FFT intensities of the $\widetilde{B}_x$ signal launched by the triangle wave antenna drive. (b) SAW-induced displacements contributed from multiple harmonics in the triangle wave drive. Triangles: experimental data with triangle wave drive; diamonds: experimental data with sine wave drive. ($\widetilde{B}_x$ data from Fig. 9, Δr data from Fig. 15.)

achieved. Primary and subordinate resonance peaks in frequency are seen in experiment and simulation. A subordinate resonance is caused by partial overlapping of the fast ion and wave phases when the frequency is an integer fraction of the primary frequency. With a pure sine wave drive, a null effect point is discovered in the resonance spectrum as predicted by theory. This null effect is absent with a triangle wave drive because higher harmonics cause an extra resonance effect. The resonance effect is kept within the linear regime where spatial displacements are proportional to the SAW amplitude. Both single-particle and Monte Carlo simulation codes proved robust in predicting the experimental results.

Several extensions of this experimental study are possible. Simulation predicts that the fast-ion beam energy is changed up to ~23 eV at the Doppler resonance condition with 1.6 G wave magnetic field amplitude. Direct measurements of energy changes could be obtained by biasing the fast-ion collector. A higher bandwidth fast-ion analyzer

would permit detection of coherent oscillations in the collector current at the wave frequency. An antenna that launches circularly polarized waves could extend the portion of the gyro-orbit that interacts with the wave, increasing the displacement. Observation over longer axial distances is also desirable.

More generally, the successful observation of fast-ion interaction with a single coherent Alfvén wave lays the groundwork for studies of more complicated wave-particle interactions, including interaction with Alfvén waves in the nonlinear regime and studies of fast-ion diffusion by drift-wave turbulence.

[1] W. W. Heidbrink, N. N. Gorelenkov, Y. Luo, M. A. Van Zeeland, R. B. White, M. E. Austin, K. H. Burrell, G. J. Kramer, M. A. Makowski, G. R. McKee, R. Nazikian, and the DIII-D Team, Phys. Rev. Lett. **99**, 245002 (2007).

[2] J. D. Evans, G. J. Morales, and R. J. Taylor, Phys. Rev. Lett. **69**, 001528 (1992).

[3] J. D. Evans, G. J. Morales, and R. J. Taylor, Ann. Isr. Phys. Soc. **190**, 242 (1989).

[4] A. J. Coates, A. D. Johnstone, R. L. Kessell, D. E. Huddleston, B. Wilken, K. Jockers, and F. M. Neubauer, J. Geophys. Res. **95**, 20701, DOI: 10.1029/JA095iA12p20701 (1990).

[5] J. V. Hollweg and P. A. Isenberg, J. Geophys. Res. **107**, 1147, DOI: 10.1029/2001JA000270 (2002).

[6] V. Shevchenko, V. Galinsky, and D. Winske, Geophys. Res. Lett. **33**, L23101, DOI 10.1029/2006GL026765 (2006).

[7] C. Z. Cheng, L. Chen, and M. S. Chance, Ann. Phys. (N.Y.) **161**, 21 (1985).

[8] W. W. Heidbrink, Phys. Plasmas **15**, 055501 (2008).

[9] K-L. Wong, Plasma Phys. Controlled Fusion **41**, R1 (1999).

[10] H. H. Duong, W. W. Heidbrink, E. J. Strait, T. W. Petrie, R. Lee, R. A. Moyer, and J. G. Watkins, Nucl. Fusion **33**, 749 (1993).

[11] R. B. White, E. Fredrickson, D. Darrow, M. Zarnstorff, R. Wilson, S. Zweben, K. Hill, Y. Chen, and G. Fu, Phys. Plasmas **2**, 2871 (1995).

[12] L. Chen, Z. H. Lin, and R. White, Phys. Plasmas **8**, 4713 (2001).

[13] R. White, L. Chen, and Z. H. Lin, Phys. Plasmas **9**, 1890 (2002).

[14] L. Zhao, W. W. Heidbrink, H. Boehmer, and R. McWilliams, Phys. Plasmas **12**, 052108 (2005).

[15] Y. Zhang, H. Boehmer, W. W. Heidbrink, R. McWilliams, D. Leneman and S. Vincena, Rev. Sci. Instrum. **78**, 013302 (2007).

[16] H. Boehmer, D. Edrich, W. W. Heidbrink, R. McWilliams, and L. Zhao, Rev. Sci. Instrum. **75**, 1013 (2004).

[17] W. Gekelman, H. Pfister, Z. Lucky, J. Bamber, D. Leneman, and J. Maggs, Rev. Sci. Instrum. **62**, 2875 (1991).

[18] T. H. Stix, *Waves in Plasmas* (American Institute of Physics, New York, 992), pp. 238–246.

[19] L. Zhao, Ph.D. thesis, University of California Irvine, 2005.

[20] A. H. Boozer, Phys. Plasmas **9**, 4389 (2002).

[21] D. Leneman, W. Gekelman, and J. Maggs, Rev. Sci. Instrum. **77**, 015108 (2006).

[22] J. E. Maggs, G. J. Morales, and T. A. Carter, Phys. Plasmas **12**, 013103 (2005).

[23] S. Vincena, Ph.D. thesis, University of California Los Angeles, 1999.

[24] Heat Wave Labs, Inc. alkali ion source doc. http://www.cathode.com/pdf/tb-118.pdf.

[25] Y. Zhang, Ph.D. thesis, University of California Irvine, 2008.

[26] UltraVolt, Inc. High Power "C"/"F" Series High Voltage Power Supply, http://www.ultravolt.com/hicser.htm.

[27] W. W. Heidbrink and J. D. Strachan, Rev. Sci. Instrum. **56**, 501 (1985).

[28] G. J. Morales, R. S. Loritsch, and J. E. Maggs, Phys. Plasmas **1**, 3765 (1994).

[29] G. J. Morales and J. E. Maggs, Phys. Plasmas **4**, 4118 (1997).

[30] W. Gekelman, D. Leneman, J. Maggs, and S. Vincena, Phys. Plasmas **1**, 3775 (1994).

[31] W. Gekelman, S. Vincena, D. Leneman, and J. Maggs, J. Geophys. Res. **102**, 7225, DOI: 10.1029/96JA03683 (1997).

[32] M. VanZeeland, W. Gekelman, S. Vincena, and G. Dimonte, Phys. Rev. Lett. **87**, 105001 (2001).

[33] N. Palmer, W. Gekelman, and S. Vincena, Phys. Plasmas **12**, 072102 (2005).

[34] T. A. Carter, B. T. Brugman, and D. W. Auerbach, CP932, *Turbulence and Nonlinear Processes in Astrophysical Plasmas, 6th Annual International Astrophysical Conference*, edited by D. Shaikh and G. P. Zank (American Institute of Physics, New York, 2007).

[35] S. Vincena, W. Gekelman, and J. Maggs, Phys. Plasmas **8**, 3884 (2001).

[36] C. Mitchell, S. Vincena, J. Maggs, and W. Gekelman, Geophys. Res. Lett. **28**, 923, DOI: 10.1029/2000GL012165 (2001).

[37] C. C. Mitchell, J. E. Maggs, and W. Gekelman, Phys. Plasmas **9**, 2909 (2002).

[38] D. Leneman, W. Gekelman, and J. Maggs, Phys. Plasmas **7**, 3934 (2000).